# Chromia layer growth on a Ni-based superalloy : sub-parabolic kinetics and the role of titanium

Cruchley, S.; Evans, Hugh; Taylor, Mary; Hardy, M. C.; Stekovic, S.

*DOI:*
10.1016/j.corsci.2013.05.016

Corrosion Science 75 (2013) 58–66

Contents lists available at SciVerse ScienceDirect

Corrosion Science

journal homepage: www.elsevier.com/locate/corsci

# Chromia layer growth on a Ni-based superalloy: Sub-parabolic kinetics and the role of titanium

S. Cruchley [a], H.E. Evans [a,*], M.P. Taylor [a], M.C. Hardy [b], S. Stekovic [c,1]

[a] School of Metallurgy and Materials, The University of Birmingham, B15 2TT Birmingham, UK
[b] Rolls-Royce plc, Elton Road, DE24 8BJ Derby, UK
[c] Linköping University, 581 83 Linköping, Sweden

ARTICLE INFO

*Article history:*
Received 17 March 2013
Accepted 21 May 2013
Available online 7 June 2013

*Keywords:*
A. Superalloys
C. Oxidation
C. Selective Oxidation

ABSTRACT

Oxidation of the Ni-based superalloy RR1000 has been undertaken in air over the temperature range 600–900 °C for times up to 5000 h. The surface oxide consisted of a protective Ti-doped chromia layer but with rutile forming on its outer surface. Sub-surface oxidation of Al and Ti also occurred. The thickening kinetics of the chromia layer were sub-parabolic with initial rates around two orders of magnitude higher than expected for Ti-free chromia. This enhancement and the sub-parabolic kinetics are accounted for by Ti-doping of the chromia layer. Over time the enhancement reduced because of Ti-depletion in the alloy.



## 1. Introduction

Nickel-based superalloys have been optimised, compositionally and microstructurally, to operate in the highly stressed conditions occurring in the hot sections of aero- or land-based gas turbine engines. The high temperatures experienced by components in these operating conditions have implications on the performance of the alloys used. Under such conditions degradation by oxidation occurs and plays a key role in determining the lifetimes of the components. One method of improving the efficiency of these engines is by increasing the operating temperatures. This will inevitably result in accelerated degradation of the alloys. For this reason it is important to understand the oxidation processes occurring and the mechanisms involved.

Superalloys used for turbine discs have operating temperatures typically $\leqslant$700 °C and form a continuous layer of chromia rather than alumina [1–5] under these conditions. This layer is often protective in that the oxygen potential beneath it is sufficient to oxidise only aluminium and titanium, of the major alloy constituents [1,3,5]. Oxides of these elements form internal, sub-surface particles, often as acicular intergranular penetrations. In addition, Ti-rich oxides are known to form on the outer surface of the chromia layer [1,3,5]. Oxidation studies on such Ni-based alloys have tended to use weight-change measurements to assess the reaction kinetics and have shown that the rate of oxidation is higher than would be anticipated for protective chromia formation [5]. This, of course, is not unexpected given that other alloy constituents (Ti and Al, in particular) are also being oxidised. It remains unclear, however, whether the chromia layer itself thickens at rates commensurate with those found on simpler alloys and pure chromium or whether the complex compositions of Ni-based alloys can lead to doping effects that produce a systematic difference in chromia growth rates. The purpose of this present work is to assess this possibility through detailed metallography of long-term oxidation specimens of the RR1000 Ni-based superalloy.

## 2. Experimental procedure

The RR1000 alloy used in this study was produced using a powder metallurgy route followed by a heat treatment to obtain a grain size of between 30 and 50 μm. The alloy has a two-phase microstructure consisting of a γ (nominally Ni,Co) matrix and approximately a 45% volume fraction of γ′ precipitates (nominally $Ni_3$[Al,Ti]). The nominal composition of the alloy was: Ni 52.3, Co 18.5, Cr 15.0, Mo 5.0, Ti 3.6, Al 3.0, Ta 2.0, Hf 0.5, Zr 0.06, C 0.027, B 0.015 wt%. This was confirmed for all elements except carbon, boron and zirconium during the course of this study using Energy Dispersion Spectroscopy (EDS).

Oxidation testing was conducted over the temperature range of 600–900 °C in laboratory air for times up to 5000 h. The size of the specimens used was approximately 20 mm by 10 mm by 2 to 5 mm thick. The specimens were cut to size using electro-dis-

* Corresponding author. Tel.: +44 (0) 121 414 5172.
*E-mail addresses:* SXC697@adf.bham.ac.uk (S. Cruchley), h.e.evans@bham.ac.uk (H.E. Evans), m.p.taylor@bham.ac.uk (M.P. Taylor), Mark.Hardy@rolls-royce.com (M.C. Hardy), svjetlana.stekovic@liu.se (S. Stekovic).
[1] Formerly, Rolls-Royce plc.

http://dx.doi.org/10.1016/j.corsci.2013.05.016
0010-938X/

**Table 1**
Test matrix showing (√) exposure times at which specimens were removed for examination. Tests marked with an * were performed using TGA rigs. The remainder of the tests were performed in static furnaces. All tests were performed in laboratory air.

| Time (h) Temp. (°C) | 24 | 50 | 100 | 300 | 500 | 1000 | 2000 | 5000 |
|---|---|---|---|---|---|---|---|---|
| 600 °C | | | | | | √ | | |
| 650 °C | | | | √* | | | | |
| 700 °C | √ | √ | √* | √ | √ | √ | √ | √ |
| 750 °C | √ | √ | √* | √ | √ | √ | √ | |
| 800 °C | √ | √ | √* | √ | √ | √ | √ | |
| 850 °C | | | √* | | | | | |
| 900 °C | | | √* | | | | | |

charge machining (EDM) and all the surfaces were ground on wet SiC paper and polished using 6 μm diamond paste to remove the damage from the EDM process and to produce a surface finish, $R_a$, of approximately 0.4 μm. All edges and corners were chamfered to reduce stress concentrators and polished to the same surface finish. The final dimensions after polishing were measured using a micrometer and the surface area calculated. Following this, the specimens were cleaned in ethanol, dried and weighed on a five figure calibrated balance.

The results from two types of oxidation test are combined in this study. Table 1 shows the test matrix with the two approaches included. All the 100 h tests and the test conducted at 650 °C were performed using a thermogravimetric balance (TGA). The weight change during these tests was monitored continually and adjusted to accommodate buoyancy effects. All other tests were conducted in horizontal tube furnaces. For these latter tests, batches of specimens were placed in alumina boats and inserted into the furnaces at temperature. Intermittent weighing at room temperature was used to determine the oxidation kinetics. At selected time intervals, a specimen was removed from the batch for examination before the high temperature exposure continued for the remainder of the batch. Table 1 shows the time intervals chosen for examination. At 600 °C one isothermal test, having an exposure time of 1000 h, has been performed to date.

After oxidation testing and re-weighing, the surfaces of the specimens were sputter coated with gold and examined by scanning electron microscopy (SEM) using both secondary (SE) and backscattered electrons (BSE). Following this, the specimens were nickel-plated and mounted in resin or vacuum impregnated in a low viscosity resin. The specimens were prepared for cross-sectional analysis by grinding on SiC papers down to 1200 grit using water as a lubricant followed by polishing using progressively finer diamond paste from 6 μm down to 0.25 μm. The cross-sections were examined using a high resolution JEOL 7000F FEGSEM. This equipment is fitted with wave-length dispersive spectroscopy (WDS), used here for the identification of oxygen and nitrogen, and EDS used for heavier element compositional identification, mapping and line scans. X-ray diffraction (XRD) analysis of the surface oxides was performed on a Philips XPert system using Cu Kα radiation, indexed between a $2\theta$ of 10–100°.

## 3. Results and discussion

### 3.1. Gravimetric oxidation kinetics

Fig. 1 shows the change in specimen weight with time over the temperature range tested. No spallation was observed for any of the specimens tested. These weight gain data were plotted (Fig. 2) according to Eq. (1) to obtain the best-fit values of '$n$', given in Table 2.

$$(\Delta m)^n = k'_n t \quad (1)$$

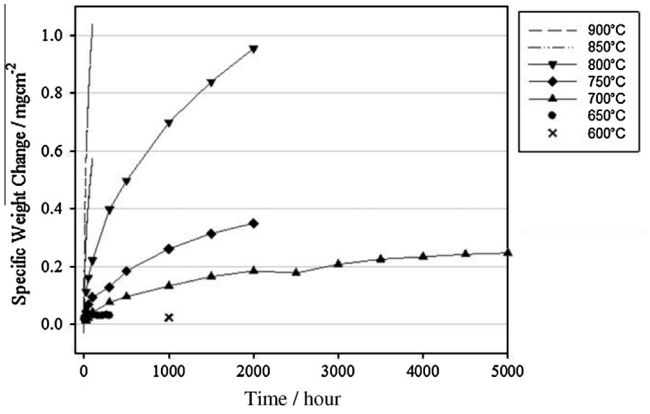


**Fig. 1.** Plot of specific weight change against time for each temperature. The data at 650, 850 and 900 °C were obtained from TGA tests, at the other temperatures the data were obtained by weighing batches of samples at 500 h interval.

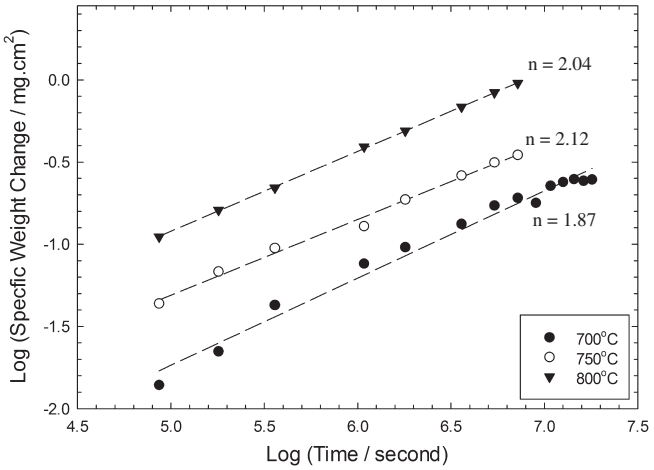


**Fig. 2.** Plot of log specific weight change against log exposure time for 700 °C, 750 °C and 800 °C showing that the weight gain kinetics can be approximated to parabolic behaviour, $n = 2$ (Eq. (1)).

**Table 2**
Best-estimate values of the exponent, $n$, (Eq. (1)) for weight gain kinetics and maximum exposure time at each temperature; n.d. – not determined.

| Temperature (°C) | $n$ | Maximum exposure time (h) |
|---|---|---|
| 900 | 2.2 | 100 |
| 850 | 2.2 | 100 |
| 800 | 2.04 | 2000 |
| 750 | 2.12 | 2000 |
| 700 | 1.87 | 5000 |
| 650 | n.d. | 350 |
| 600 | n.d. | 1000 |

Here $(\Delta m)$ is the specific weight gain in mg cm$^{-2}$, $t$ is exposure time in seconds and $k'_n$ is a rate constant. It can be appreciated from Table 2 that the values of n, at least at the highest temperatures, are sufficiently close to 2 that parabolic kinetics can be assumed, i.e. $n = 2$ in Eq. (1) and $k'_n = k'_p$, the parabolic rate constant expressed in terms of weight gain. It was assumed that parabolic conditions also obtained for the two lowest temperatures used although the data were limited at these temperatures. The parabolic rate constants calculated from Eq. (1) for all temperatures used in the present work are shown in the second column of Table 3. Also shown in Table 3, in the third column, are the parabolic rate constants determined from relatively short-term (100 h) tests,

**Table 3**
Weight gain parabolic rate constants determined from Fig. 2 and from an earlier study [5].

| Temperature (°C) | $k_p'$ (mg$^2$ cm$^{-4}$ s$^{-1}$) this study | $k_p'$ (mg$^2$ cm$^{-4}$ s$^{-1}$) from earlier study [5] |
|---|---|---|
| 900 | – | $3.13 \times 10^{-6}$ |
| 850 | – | $9.32 \times 10^{-7}$ |
| 800 | $1.22 \times 10^{-7}$ | $1.86 \times 10^{-7}$ |
| 750 | $1.74 \times 10^{-8}$ | $3.15 \times 10^{-8}$ |
| 700 | $3.59 \times 10^{-9}$ | $3.23 \times 10^{-9}$ |
| 650 | $8.22 \times 10^{-10}$ | – |
| 600 | $1.60 \times 10^{-10}$ | – |

**Table 4**
Activation energies for RR1000 determined in this study and from results on other relevant alloys available in the literature.

| Alloy | Activation energy (kJ mol$^{-1}$) | References |
|---|---|---|
| Coarse-Grained RR1000 | 286 | This study |
| Fine-Grained RR1000 | 270 | [4] |
| Udimet 720 | 250 | [1] |
| Astroloy | 270 | [1] |
| Waspaloy | 300 | [1] |
| Chromium/20Cr austenitic steel | 258 | [6] |

as reported previously [5]. The values at the three common test temperatures of 700, 750 and 800 °C in the two studies are similar but the present values are considered more reliable since they were obtained from longer-term exposures. The previous results from the higher test temperatures (850 and 900 °C) were incorporated into the present data set, however, since the higher temperatures permitted appreciable weight gains even with the shorter times used (Fig. 1) and, being TGA tests, some 500 data points were used in the evaluation of '*n*'.

The parabolic rate constants for weight gain are shown as a function of the inverse of the temperature in the Arrhenius plot of Fig. 3 for the present specimens and for related alloys [1,4,6–9]. The gradient of the line through the present results yields an "activation energy" of 286 kJ mol$^{-1}$ to give an expression for $k_p'$ of:

$$k_p' = 1.73 \times 10^7 \exp\left[-\frac{286076}{8.314T}\right], \text{mg}^2\ \text{cm}^{-4}\ \text{s}^{-1} \quad (2)$$

where $T$ is temperature in *K*. This equation is plotted as the broken line in Fig. 3. It should be noted that although the term "activation energy" is used here, this is not rigorously correct since more than one alloy constituent is being oxidised and a single activated event is not being studied. Nevertheless, it remains a useful way of describing the temperature dependence of the reaction kinetics.

The value for the activation energy found here is lower than that of 320 kJ mol$^{-1}$ obtained from the short-term tests of the earlier study [5] but is more in keeping with that determined from other alloys of similar composition [1,4], Table 4. In general, however, the activation energies for the superalloys tend to be somewhat higher than that reported elsewhere [6] for the growth of a chromia layer (258 kJ mol$^{-1}$) on pure chromium and an austenitic steel. The expected $k_p'$ values for chromia growth on this simple austenitic steel are shown as the solid line in Fig. 3. These rate constants, expressed in terms of weight gain, were obtained from the original metallographic data [6] by equating 1 mg cm$^{-2}$ weight gain to a chromia layer thickness of 6.0 μm. This calculated line tends to form a lower bound to the superalloy data.

### 3.2. Oxide characterisation

The typical oxide morphology is shown in the cross-section of Fig. 4 from which it can be seen that both surface and internal oxides formed in this alloy. EDS analysis confirmed that the external surface oxides were chromium- and titanium-rich and that subsurface alumina was also formed, Fig. 5. These alumina penetrations occurred to greater depths at the alloy grain boundaries and this, along with the enhanced surface oxidation noted previously [5] at emerging alloy grain boundaries, demonstrated that these sites were, as expected, paths of faster diffusion. In addition, sub-surface nitrides of titanium formed ahead of the zone of alumina formation. Fig. 6a shows EDS maps of a sub-surface region including a grain boundary, showing that, ahead of the alumina penetration, titanium-rich phases were formed at the grain boundary and within the grains. No oxygen can be seen in the EDS maps associated with the titanium in these regions but WDS analysis has confirmed that nitrogen is present (Fig. 6b and Table 5).

Closer examination of the EDS maps of Fig. 5 reveals that the chromium-rich surface oxide layer contained detectable amounts of titanium, in addition to there being a separate outer region of titanium-rich oxide. XRD spectra obtained from the surface oxide layer are shown in Fig. 7 for specimens exposed for 100 h at each of 700, 750 and 800 °C. It can be inferred from the identified peaks, together with the EDS results, that the outermost surface contained crystals of rutile ($TiO_2$) but that the thicker chromium-rich oxide layer was chromia even though titanium was also present.

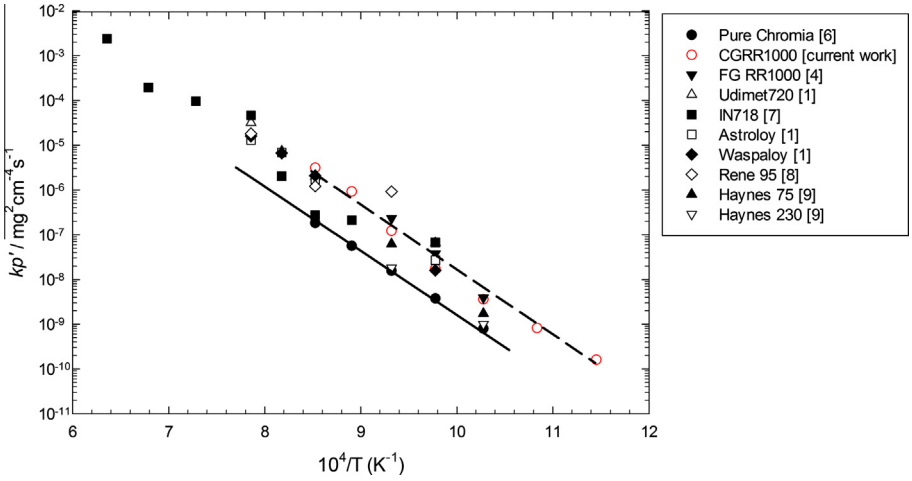


**Fig. 3.** Arrhenius plot of $k_p'$ values from this study (shown as unfilled circles) and from various superalloys taken from the literature (compiled in [5]). Also shown as the solid line are the expected $k_p'$ values for chromia growth [6] on simpler alloys. All exposures were undertaken in laboratory.

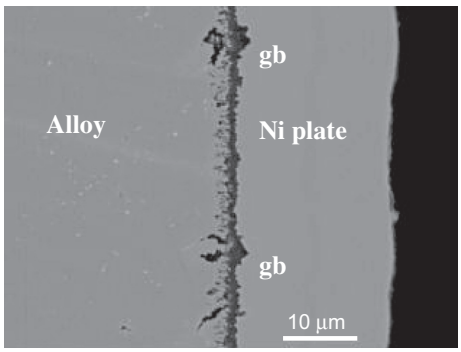


**Fig. 4.** Back Scattered Electron (BSE) image of a cross-section through a sample held at 750 °C for 1000 h showing the formation of a continuous external oxide with sub-surface oxide penetration into the alloy. Grain boundaries (g.b.) were found to be sites of enhanced external oxide growth and greater alloy penetration depths.

The ability of chromia to dissolve titanium in the oxidised state has been known for some time [10–12]. It is likely that titanium is incorporated as the $Ti^{4+}$ ion since this has minimal effect on the chromia lattice spacing, even at high dopant levels [10] which is consistent with the present XRD observations. The phase equilibrium data of Naoumidis et al. [11] suggest that, for their test temperature of 1000 °C, titanium solubility decreases with increasing oxygen partial pressure ($pO_2$) and is insignificant for $pO_2 > 10^{-18}$. At higher pressures the $Cr_2Ti_3O_9$ phase would be expected. This phase has a principal XRD peak at $2\theta \sim 28.5°$ [13] but no evidence was found for this in the present work (Fig. 7) even though the specimens were tested in air ($pO_2 \sim 0.21$). It suggests, reasonably, that the solution characteristics of titanium in the chromia layer are determined by the $pO_2$ existing at the chromia/alloy interface where the solution process takes place. The oxygen partial pressure here will be much less than $10^{-18}$ at the present test temperatures.

Sub-surface oxides could not be detected with confidence in these XRD scans because of their small volume fraction although peaks associated with the substrate alloy were present.

### 3.3. Chromia growth kinetics

The oxidation of elements other than chromium together with the formation of titanium nitrides and localised enhanced oxide growth at grain boundaries will increase the oxidation weight gain above that expected simply for the formation of a uniform layer of chromia. To confirm whether these factors accounted for the higher weight-gain parabolic rate constants found (Fig. 3), chromia thickness measurements were taken from sections through the tested specimens. A total of 50 measurements was made from ten micrographs of representative images of each specimen as shown in Fig. 8. This approach was complicated by the change in the surface profile of the alloy that occurred during oxidation (Fig. 8) and by the formation of $TiO_2$ above the chromia layer (Figs. 5 and 8b). To aid these chromia measurements, EDS maps (Fig. 5, for example) were taken for every condition of exposure time and temperature and used to differentiate between chromia and rutile.

Fig. 8a shows a cross-section through a specimen and demonstrates the flat surface profile that existed prior to oxidation testing. With increasing exposure time, however, a highly non-planar oxide/metal interface progressively developed (Fig. 8b) consisting of protuberances and metallic regions within the oxide layer. This morphology may have developed as a result of undercutting by oxide formation [14] or actual protuberances may have developed. In the latter case, they could have been formed by outward alloy

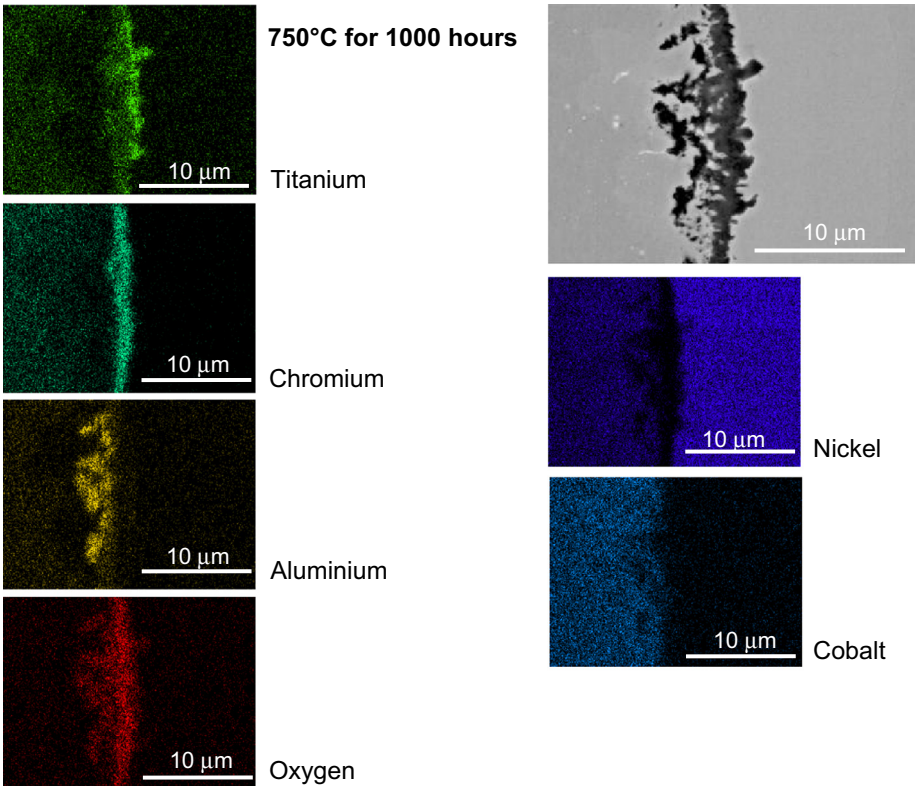


**Fig. 5.** BSE image and EDS maps of a section through a specimen held at 750 °C for 1000 h showing the distribution of elements in the oxides formed, as indicated by the presence of oxygen.

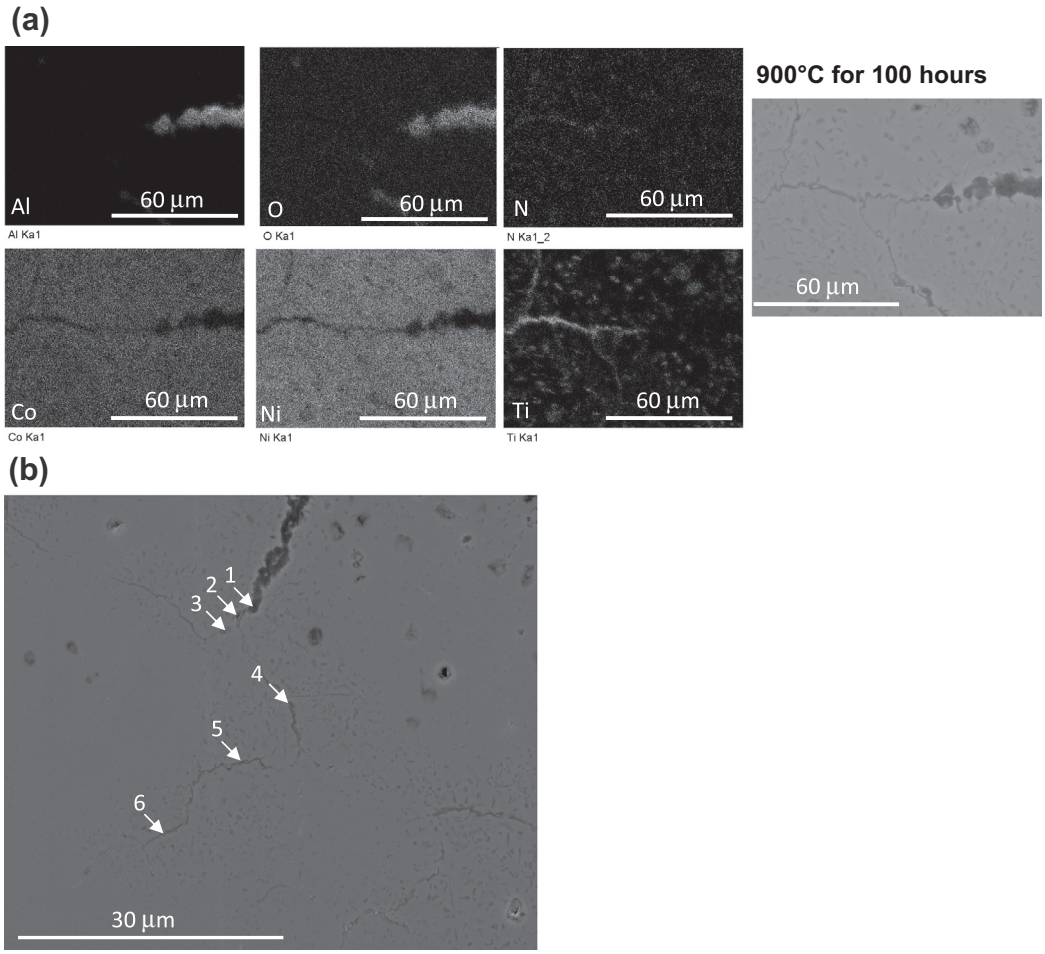


**Fig. 6.** (a) High magnification back scattered electron image and EDS maps showing a sub-surface region with alumina penetration along a grain boundary, on the right, and a titanium-rich phase ahead of this; (b) SEM image of adjacent area showing the location of sites where WDS/EDS analyses were performed, the results of which are presented in Table 5.

**Table 5**
Analysis of the positions indicated in Fig. 6b in atomic %. Nitrogen and oxygen values were obtained using WDS, all other elements determined using EDS. Minor amounts of molybdenum, hafnium and tantalum were also detected. Note that substantial matrix signals were obtained when examining small particles.

| Position | N | O | Al | Ti | Cr | Co | Ni |
|---|---|---|---|---|---|---|---|
| 1 | 0 | 42.6 | 24.3 | 4.4 | 4.7 | 7.0 | 16.4 |
| 2 | 0 | 31.1 | 15.3 | 6.4 | 6.5 | 10.0 | 23.9 |
| 3 | 0 | 22.4 | 17.0 | 3.2 | 8.3 | 13.4 | 34.6 |
| 4 | 10.5 | 0 | 1.1 | 24.4 | 10.5 | 14.6 | 36.6 |
| 5 | 5.9 | 0 | 3.0 | 7.0 | 12.9 | 19.6 | 48.8 |
| 6 | 7.9 | 0 | 1.6 | 10.1 | 13.0 | 18.5 | 46.4 |

creep to accommodate the increase in volume resulting from internal oxide formation, as has been suggested for other alloy systems e.g. [15–19]. The exact composition of these metallic regions was difficult to determine due to their relatively small size compared with the resolution of the SEM probe but EDS analysis showed them to be cobalt- and nickel-rich, being depleted of aluminium, titanium and chromium. This demonstrates that the chromia layer was protective in that the oxygen partial pressure at its base was sufficient to oxidise aluminium and titanium but not to form oxides of lower thermodynamic stability such as CoO and NiO.

With increasing exposure time, the metallic regions could appear to become isolated from the alloy, as can be seen in Fig. 8b, although there may be connectivity with the alloy in the third dimension. Interestingly, the presence of these features did not appear to affect the thickness of the external oxide scale significantly, as can be appreciated from Fig. 8b. Accordingly, no allowance was made during measurement for the presence or absence of these features on the occasions when measurement sites intersected them. In addition no account was made for the small fraction of isolated voids that were encountered. It is estimated that the overall error on chromia thickness due to these factors was an overestimate of <3%.

Typical kinetics for chromia thickening are shown in Fig. 9 for the exposures at 750 °C, as an example, and compared there with the expected chromia thicknesses grown on pure chromium and an austenitic steel [6] according to the following equation:

$$k_p = 2.07 \times 10^{-2} \exp\left[-\frac{31020}{T}\right], \mathrm{cm^2\ s^{-1}} \quad (3)$$

Here $k_p$ is the parabolic rate constant for chromia growth defined as:

$$k_p = \frac{\xi^2}{t} \quad (4)$$

where $\xi$ is the thickness of the oxide layer and $t$ is exposure time. From this comparison, it can be appreciated that the chromia growth rate observed on the superalloy was significantly greater than that expected from chromia growth on simpler Ti-free alloys or for adherent scales on pure chromium. Whereas, for the latter

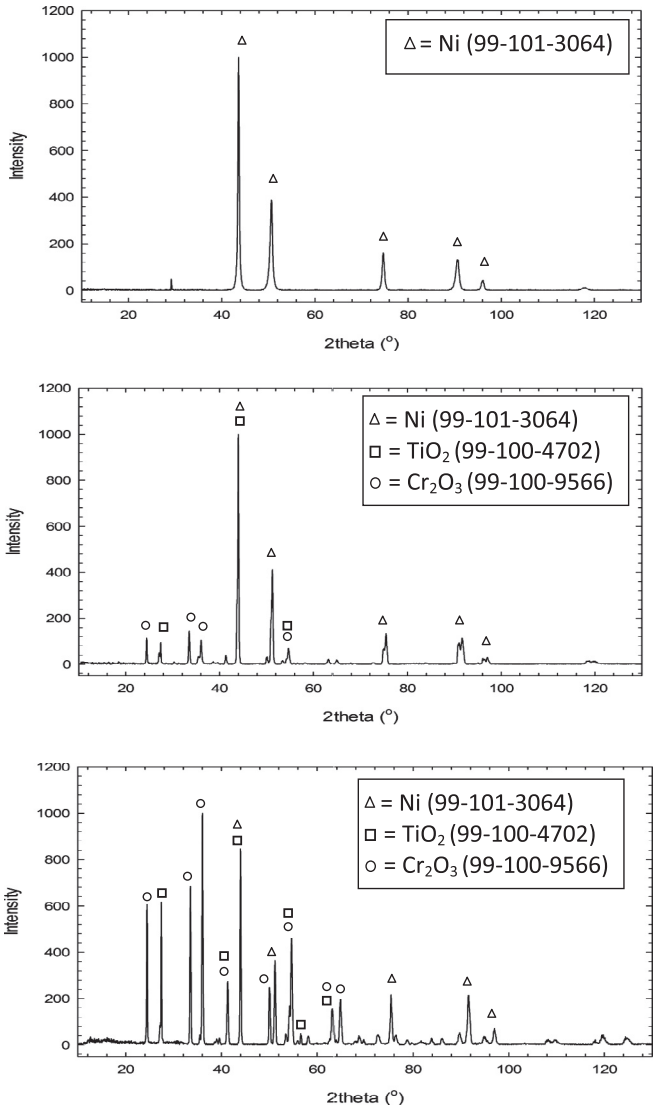


**Fig. 7.** XRD traces of specimens held at (a) 700 °C, (b) 750 °C and (c) 850 °C, for 100 h with identification of the peaks between a $2\theta$ of 10–100°. The key contains the ICDD card number of the phases identified.

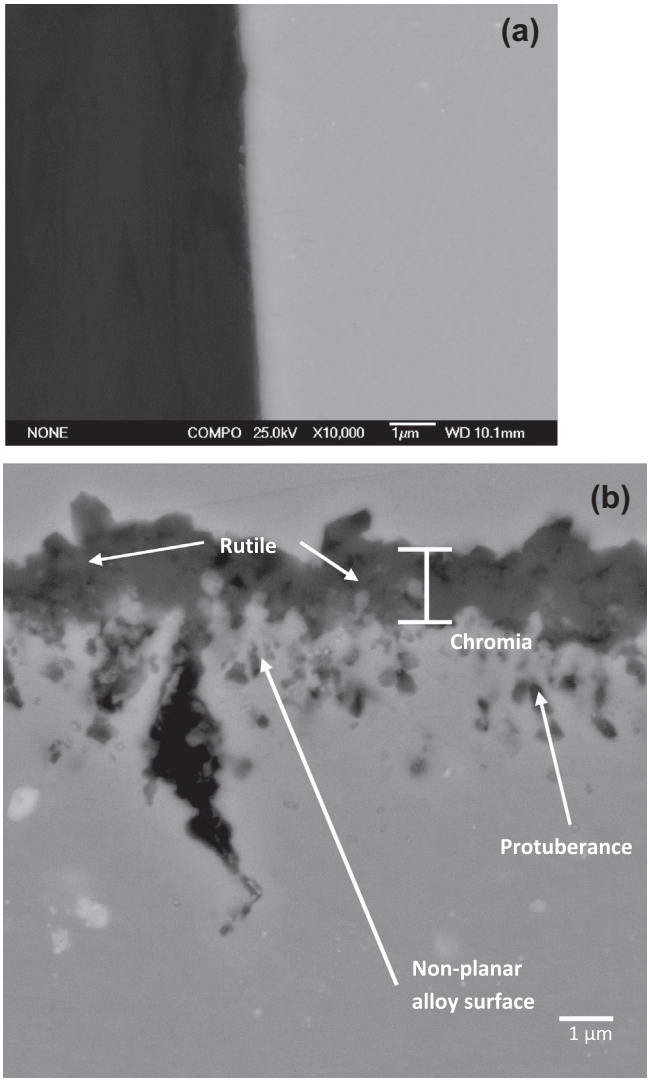


**Fig. 8.** (a) BSE image through a section of a specimen prior to oxidation testing showing the relatively flat surface profile; (b) BSE image at similar magnification of a cross-section through a specimen held at 750 °C for 1000 h illustrating that the oxide/metal interface becomes non-planar and how oxide thickness measurements were performed.

cases, parabolic conditions obtained, the chromia layer on the present alloy grew sub-parabolically with a time exponent, $(1/m)$ in Eq. (5), of ~0.3.

$$\xi = (k_m t)^{1/m} \tag{5}$$

where $k_m$ is an effective rate constant. Sub-parabolic kinetics have recently also been reported on the similar Ni-based superalloy, ME3 [20].

The best-fit values for $k_m$ and $(1/m)$ at each of the three test temperatures at which detailed metallographic measurements were made are given in Table 6. In each case, the chromia growth rates in the present RR1000 alloy were higher than for those on simpler alloys. This increase in rate can be quantified from the slope, $d\xi/dt$, of the chromia-thickness/time curves and by evaluating the ratio, '*r*', of that for the current superalloy (subscript '*s*' in Eq. (6)) and that for the simpler alloy and chromium (subscript '*cr*'):

$$r = \left(\frac{(d\xi/dt)_s}{(d\xi/dt)_{cr}}\right)_\xi \tag{6}$$

This ratio needs to be evaluated at a given oxide thickness, $\xi$, as indicated in Eq. (6), to ensure the comparison is made at a given diffusion distance for the chromium defects transporting across the oxide layer. The calculation of the ratio '*r*' was made using the best-fit equations for the simple alloy/chromium (Eqs. (3) and (4)) and for the superalloy at each of the three principal test temperatures using the parameters given in Table 6. The dependence of the ratio '*r*' on oxide thickness and test temperature is shown in Fig. 10. From this, it is clear that the ratio at all three temperatures is very high initially, indicating that the rate of defect transport across the chromia layer on the superalloy is some two orders of magnitude faster than the simpler alloy at an oxide thickness of 0.1 μm. It appears that the enhancement ratio is somewhat higher at the lower test temperatures but, in all cases, the ratio decreases rapidly with increasing oxide thickness. At an oxide thickness of 2 μm, the enhancement ratio has reduced to approximately 6 for the 800 °C test data but is similar for all three test temperatures.

It has been recognised in various studies [1,3,5,12,20–25] that titanium, as an alloy constituent, can have a deleterious effect on

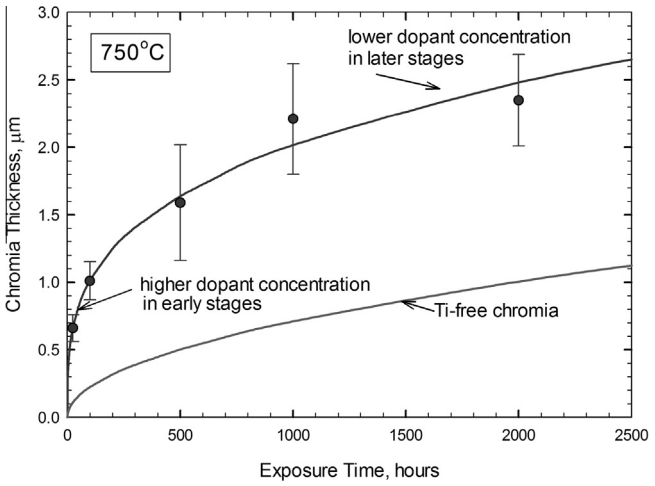


**Fig. 9.** Plots of chromia thickness measured on the present superalloy at 750 °C compared with the predicted chromia thickness obtained on Ti-free austenitic steel/ pure chromium [6]. Oxide thickness measurements for RR1000 were normally distributed and error bars are shown as ±1 standard deviation.

**Table 6**
Kinetic parameters for the thickening of the chromia layer on RR1000. See the text for the definition of '$m$' and '$k_m'$'. Units are µm and seconds.

| Temperature (°C) | $(1/m)$ | $k_m$ ($\mu m^m s^{-1}$) |
|---|---|---|
| 800 | 0.343 | 0.0197 |
| 750 | 0.299 | 0.0221 |
| 700 | 0.311 | 0.0130 |

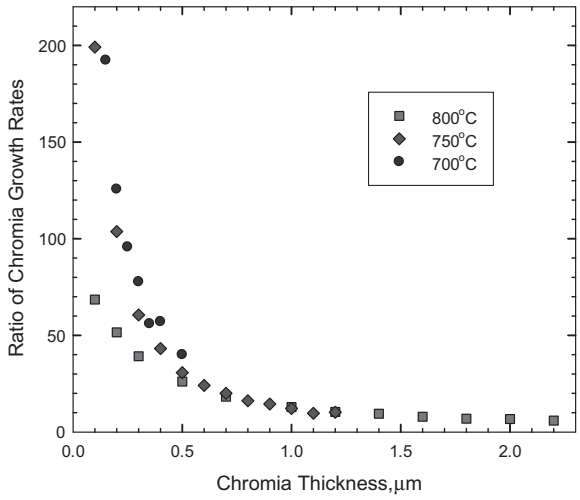


**Fig. 10.** The variation of the enhancement ratio with oxide thickness for the three test temperatures at which extensive oxide thickness measurements were undertaken. See text for further details.

oxidation resistance and is known to act both through an impairment of oxide adherence and through the formation of Ti-rich oxides. Rutile formation has also been demonstrated in this study although no evidence of oxide spallation was observed. The striking feature of the present work was the large enhancements found in chromia growth rates and it is suggested that this is also a further deleterious effect of titanium, associated with its retention within the chromia layer (Fig. 5). A plausible explanation is that this titanium addition acts as a higher-valent dopant to increase the concentration of chromium vacancies [12,25–27]. This possibility has been considered in detail by Atkinson et al. [10,27] in the context of Ti-doped chromium oxide used in sensors for trace gases. A 4-valent titanium ion can be considered to enter the chromia lattice via the dissociation of $TiO_2$ according to:

$$3TiO_2 \rightarrow 3Ti_{Cr}^{\cdot} + V_{Cr}''' + 6O_O^x \quad (A)$$

where the first term on the right-hand side of reaction (A) represents the excess positive charge associated with the titanium ion located on a chromium lattice site; $V_{Cr}'''$ is a triply charged Cr vacancy; $O_O$ is the oxygen ion on the oxygen sub-lattice. It should be noted that this simple reaction envisages single chromium vacancies but it may be that these, in fact, form clusters with the titanium ion [10,27]. The actual defect structure of Ti-doped chromia is unclear but an increase in chromium vacancies is expected as a result of the incorporation of a higher-valent ion. It needs to be assumed, of course, that such concepts will also apply to the oxide grain boundaries since these are likely to remain the main diffusion routes at the temperatures used in this present work. These excess vacancies will increase oxidation rates through increasing the diffusion rates of the chromium ion across the oxide layer. It is not possible to quantify this in this work since the titanium concentration within the chromia layer could not be determined reliably using the SEM because of the thinness of the oxide layer and the proximity of the outer layer of rutile (Fig. 5). Nevertheless, relatively small quantities of dopant are expected to have a significant effect since the intrinsic vacancy defect population within pure chromia will be small.

Finally, it should be recognised that the *average* quantity of titanium dopant within the chromia layer is likely to decrease as the layer thickens because of the depletion of the element in the adjacent alloy. Fig. 11 shows SEM images with EDS traces for two exposures at 800 °C, (a) 200 h, (b) 2000 h. In both, the locations of the external oxides, γ′ denuded zones and the alloy are labelled. The γ′ denuded zone after 2000 h exposure at 800 °C is shown in Fig. 12. It can be seen in Fig. 11a, within the γ′ denuded zone, there is some depletion of titanium and aluminium immediately adjacent to the external oxide. In (b) the titanium and aluminium concentration, within the γ′ denuded zone, is essentially zero. The width of the titanium depletion zone is estimated to have increased from 1 µm to 13 µm over this exposure period.

In Fig. 11 the gradient of the titanium concentration adjacent to the external oxide at 200 h is positive, indicating that there is a flux of titanium into the growing external oxide. At 2000 h, however, the gradient at the interface approaches zero and, thus, the driving force for the diffusion of titanium atoms is greatly reduced as is the flux of titanium into the oxide. This will result in a decreasing rate-enhancement ratio with increasing oxide thickness, as observed (Fig. 10). It will also ensure that sub-parabolic growth kinetics (e.g. Fig. 9) will result [12] since the average chromium diffusion coefficient within the oxide will also reduce with increasing oxide thickness.

## 4. Conclusions

An oxidation study has been conducted over the temperature range 600 to 900 °C for times up to 5000 h, on the nickel-based alloy RR1000 exposed to air. The main findings of the work are itemised below.

(1) The weight gain kinetics are essentially parabolic with an effective "activation energy" of the parabolic rate constant of ~286 kJ mole$^{-1}$. This is similar to the values found for other chromia-forming superalloys, as reported in the literature.

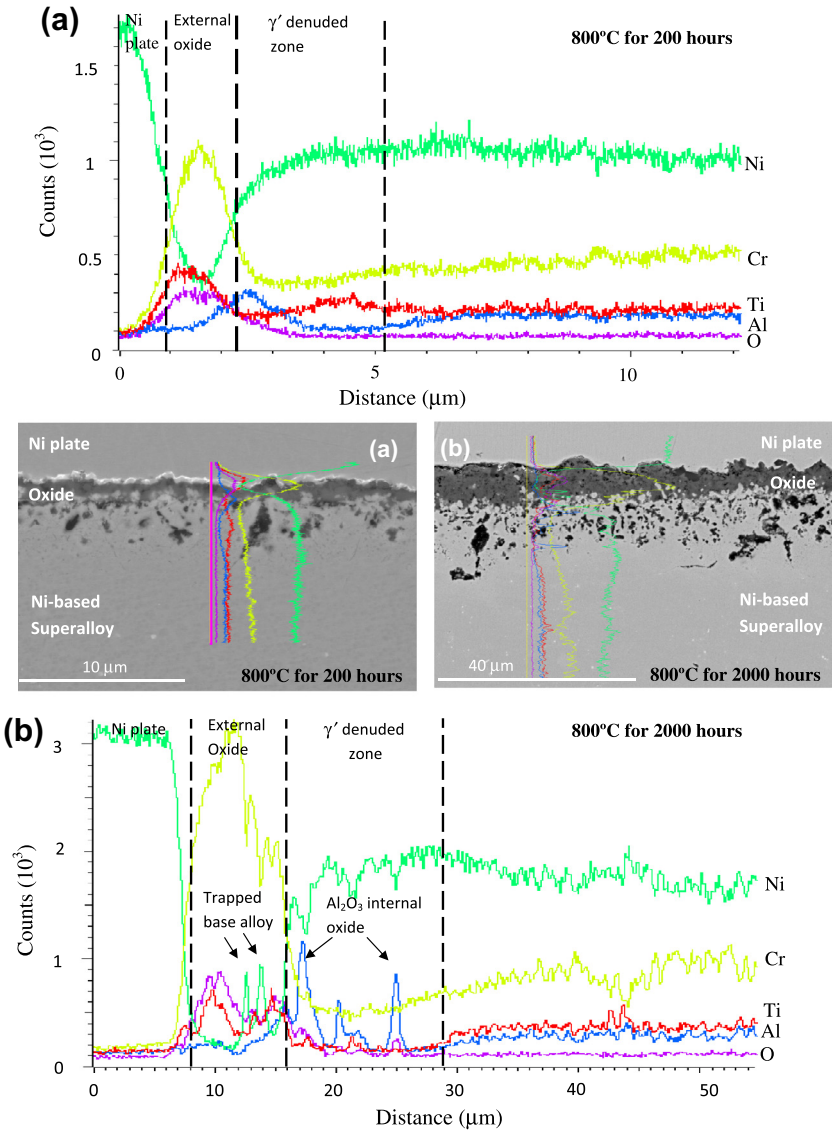


**Fig. 11.** EDS linescans (and BSE images) of RR1000 oxidised isothermally at 800 °C for: (a) 200 h and (b) 2000 h showing titanium and aluminium depletion underlying the external oxide scale.

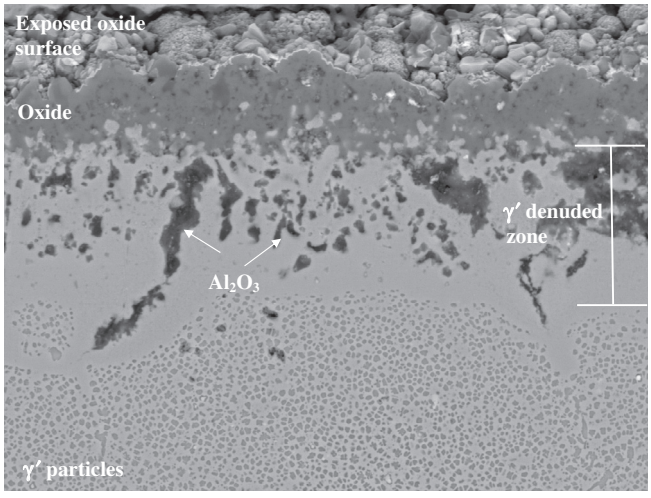


**Fig. 12.** BSE image of the γ′ denuded zone of an etched RR1000 specimen oxidised isothermally at 800 °C for 2000 h. The composition of the selective γ′ etchant is described in [28].

(2) The oxide formed at all test temperatures consists of a surface layer of chromia with discrete crystals of rutile on its outer surface. The chromia layer contains titanium but exhibits protective behaviour in that only aluminium and titanium oxidise beneath it. Titanium nitride forms ahead of the alumina penetrations, particularly at the alloy grain boundaries.

(3) The growth rate of the chromia surface layer is significantly greater, at around two orders of magnitude for thin (~0.1 μm) layers, than that observed elsewhere on a simpler Ti-free austenitic steel and also for adherent scales on chromium. This high enhancement ratio reduces with increasing oxide thickness to a value of ~6 at a layer thickness of 2 μm. The increased oxidation rate in the present alloy is attributed to increased ionic transport caused by doping of the chromia layer by titanium and the consequent creation of vacancies on the chromium sub-lattice.

(4) The growth kinetics of the chromia layer are sub-parabolic reflecting the decreasing enhancement ratio with increasing oxide thickness. It is likely that this is caused by a reduction

in the average titanium content within the oxide as continued scale growth depletes the underlying alloy of the element.

## Acknowledgment

The authors are grateful for the financial support of the Engineering and Physical Sciences Research Council and of Rolls-Royce plc.

## References

[1] J. Chen, P. Rogers, J.A. Little, Oxidation behavior of several chromia-forming commercial nickel-base superalloys, Oxid. Met. 47 (1997) 381–410.
[2] F.A. Khalid, S.E. Benjamin, The effect of deformation substructure on the high-temperature oxidation of Inconel 625, Oxid. Met. 54 (2000) 63–71.
[3] D. Kim, C. Jang, W. Ryu, Oxidation characteristics and oxide layer evolution of Alloy 617 and Haynes 230 at 900 °C and 1100 °C, Oxid. Met. 71 (2009) 271–293.
[4] A. Encinas-Oropesa, N.J. Simms, J.R. Nicholls, G.L. Drew, J. Leggett, M.C. Hardy, Evaluation of oxidation related damage caused to a gas turbine disc alloy between 700 and 800 °C, Mater. High Temp. 26 (2009) 241–249.
[5] M.P. Taylor, H.E. Evans, S. Stekovic, M.C. Hardy, The oxidation characteristics of the Ni-based superalloy, RR1000, at temperatures 700–900 °C, Mater. High Temp. 29 (2012) 145–150.
[6] H.E. Evans, D.A. Hilton, R.A. Holm, S.J. Webster, The influence of a titanium nitride dispersion on the oxidation behavior of 20%Cr–25%Ni stainless steel, Oxid. Met. 12 (1978) 473–485.
[7] G.A. Greene, C.C. Finfrock, Oxidation of Inconel 718 in air at high temperatures, Oxid. Met. 55 (2001) 505–521.
[8] L. Zheng, M. Zhang, J. Dong, Oxidation behavior and mechanism of powder metallurgy Rene95 nickel based superalloy between 800 and 1000 °C, Appl. Surf. Sci. 256 (2010).
[9] B.R. Barnard, P.K. Liaw, R.A. Buchanan, D.L. Klarstrom, Effects of applied stresses on the isothermal and cyclic high-temperature oxidation behavior of superalloys, Mater. Sci. Eng. A 527 (2010) 3813–3821.
[10] A.N. Blacklocks, A. Atkinson, R.J. Packer, S.L.P. Savin, A.V. Chadwick, An XAS study of the defect structure of Ti-doped α-$Cr_2O_3$, Sol. State Ionics 177 (2006) 2939–2944.
[11] A. Naoumidis, H.A. Schulze, W. Jungen, P. Lersch, Phase studies in the chromium-manganese-titanium oxide system at different oxygen partial pressures, J. Eur. Ceram. Soc. 7 (1991) 55–63.
[12] P.J. Ennis, W.J. Quadakkers, Corrosion and creep of nickel-base alloys in steam reforming gas, in: J.B. Marriot, M. Merz, J, Nikoul, J. Ward (Eds.), High temperature alloys – Their exploitable potential, Elsevier London, 1988, pp. 465–474.
[13] K. El-Menshawy, H.P. Buchkremer, F. Tietz, D. Stoever, Electrical conductivity of sintered chromia mixed with $TiO_2$, CuO and MnO-oxides, J. Mater. Sci. Technol. 22 (2006) 245–251.
[14] G.C. Wood, T. Hodgkiess, D.P. Whittle, A comparison of the scaling behaviour of pure iron-chromium and nickel–chromium alloys in oxygen, Corr. Sci. 6 (1966) 129–147.
[15] I.M. Edmonds, H.E. Evans, C.N. Jones, The role of the γ′ precipitate dispersion in forming a protective scale on Ni-based superalloys at 750 °C, Oxid. Met. 73 (2010) 193–206.
[16] J. Issartel, S. Martoia, F. Charlot, V. Parry, G. Parry, R. Estevez, Y. Wouters, High temperature behavior of the metal/oxide interface of ferritic stainless steels, Corr. Sci. 59 (2012) 148–156.
[17] H. Ackermann, G. Teneva-Kosseva, K. Lucka, H. Koehne, S. Richter, J. Mayer, Oxidation behaviour of selected wrought Ni-base high temperature alloys when used as flame tube material in modern blue flame oil burners, Corr. Sci. 49 (2007) 3866–3879.
[18] P. Huszkowski, S. Ertl, J. Piron-Abellan, N. Christiansen, T. Höfler, V. Shemet, L. Singheiser, W.J. Quadakkers, Effect of component thickness on lifetime and oxidation rate of chromia forming ferritic steels in low and high pO2 environments, Mater. High Temp. 22 (2005) 253–262.
[19] D.J. Young, Predicting internal oxidation: Building on the Wagner model, Mater. Sci. Forum 696 (2011) 1–11.
[20] C.K. Sudbrack, S.L. Draper, T.T. Gorman, J. Telesman, T.P. Gabb, D.R. Hull, Oxidation and the effects of high temperature exposures on notched fatigue life of an advanced powder metallurgy disk superalloy, in: E.S. Huron, R.C. Reed, et al. (Eds.), Superalloys 2012: 12th International Symposium on Superalloys, TMS, Hoboken, New Jersey, USA, 2012, pp. 863–872.
[21] H. Nagai, M. Okabayashi, H. Mitani, The effects of rare earths and reactive elements on the oxidation resistance of Ni–20Cr alloy, Trans. Japan Inst. Met. 21 (1980) 341–348.
[22] F.H. Stott, S. Berg, M. Sang, N. Karim, The oxidation performance of superalloys in gaseous environments at very high temperatures, in E. Bachelet, et al. (Eds.), High Temperature Materials for Power Generation, Kluwer Academic Publishers, 1990, pp. 213–226.
[23] A. Strawbridge, H.E. Evans, C.B. Ponton, Spallation of oxide scales from NiCrAlY overlay coatings, in: R. Streiff, J. Stringer, et al. (Eds.), High Temperature Corrosion and Protection of Materials 4, Trans Tech Publications, Zurich, Switzerland, 1997, pp. 365–372.
[24] B. Gleeson, M.A. Harper, Effects of minor alloying additions on oxidation behaviour of chromia-forming alloys, in: M. Schütze, W.J. Quadakkers, J.R. Nicholls (Eds.), Lifetime Modelling of High Temperature Corrosion Processes: (EFC 34), Maney Publishing, London, 2001, pp. 167–177.
[25] H. Buscail, S. Perrier, C. Josse, Oxidation mechanism of the Inconel 601 alloy at high temperatures, Mater. Corros. 62 (2011) 416–422.
[26] A. Holt, P. Kofstad, Electrical conductivity of $Cr_2O_3$ doped with $TiO_2$, Sol. State Ionics 117 (1999) 21–25.
[27] A. Atkinson, M.R. Levy, S. Roche, R.A. Rudkin, Defect properties of Ti-doped $Cr_2O_3$, Sol. State Ionics 177 (2006) 1767–1770.
[28] Z.W. Huang, H.Y. Li, M. Preuss, M. Karadge, P. Bowen, S. Bray, G. Baxter, Inertia friction welding dissimilar Ni-based superalloys Alloy 720Li to IN718, Metall. Mater. Trans. A 38A (2007) 1608–1620.